Contrast Attenuation Factors for Remote Sensing

Attenuation factors for the contrast of objects lying on the earth's surface and observed through five different atmospheric models are calculated as a function of the wavelength (0.31–0.9935 µm), solar zenith angle, ground reflectivity, and the nadir and azimuth angles of view. The first model is free of aerosols and absorbing gases. Absorption by average amounts of oxygen, ozone, and water vapor is included in the remaining four models. The second model is also free of aerosols, but the last three models contain aerosols in the form of a spherical polydispersion made from a substance with a spectrally independent refractive index of 1.5–0.01 i. Models 3 and 4 are expected to represent, respectively, the average and strong turbid conditions encountered over large continental areas. Models 3 and 5 contain aerosols with different size distribution characteristics, but have the same amount of aerosol mass loading per unit horizontal area. The contrast attenuation factor is found to increase with an increase in wavelength and reflectivity of the surrounding surface, and a decrease in the atmospheric turbidity and gaseous attenuation. It also depicts strong azimuthal dependence especially for models illuminated by low-altitude solar radiation of longer wavelengths.

Introduction

The Landsat (formerly known as ERTS) satellites launched by the U.S. National Aeronautics and Space Administration (NASA) during 1972 and 1975 are equipped to provide a high-resolution spatial mapping of the earth-atmosphere system in four different spectral bands [1], namely, 0.5-0.6 μ m, 0.6-0.7 μ m, 0.7-0.8 μ m, and $0.8-1.1 \mu m$. A very significant portion of these data could be used in several diverse applications such as crop census, identification of vegetation disease, fish production, sea state and ice conditions, water resources inventory, pollution monitoring, and geological surveys [2-4]. However, a full use of the short-wavelength portion of these multispectral data is hindered, to some extent, by difficulties in correcting signals for atmospheric attenuation effects. These effects are highly variable and depend upon a number of parameters such as the atmospheric composition, wavelength of observation, solar zenith angle, and the nadir and azimuth angles of the direction of observation, i.e., the view angle. Even though an accurate determination of these attenuation effects for specified atmospheric conditions and observational geometry is feasible, computer time limitations have dictated the use of approximate solutions of the radiative transfer equation for rather crude atmospheric models [5, 6].

The Landsat 3 satellite, launched by NASA in March of 1978, contains an additional spectral band in the 10.4-12.6-µm region. This is the atmospheric window region, so called because the transmission of the ground signal is least affected by attenuation due to gases and aerosols. However, this spectral band does contain a weak ozone band and a continuum of strong absorption bands for water vapor and carbon dioxide on both sides of the window region [7]. Furthermore, scattering by large aerosol particles and fog droplets can also play a significant role in the modulation of the ground signal. We exclude any further discussion of this infrared band in this paper, since it is a very complex problem involving emission, absorption, and scattering in a nonhomogeneous atmosphere.

A nonluminous object situated at the earth's surface and its surrounding background are illuminated by direct, as well as diffuse, solar radiation. Because of the differences in the reflecting properties of the object and its surroundings, an observer situated at the earth's surface distinguishes them by measuring the ratio of the difference between these brightnesses to the brightness of the background. This ratio is called the intrinsic contrast. The same object and background, when viewed by an ob-

Copyright 1979 by International Business Machines Corporation. Copying is permitted without payment of royalty provided that (1) each reproduction is done without alteration and (2) the *Journal* reference and IBM copyright notice are included on the first page. The title and abstract may be used without further permission in computer-based and other information-service systems. Permission to *republish* other excerpts should be obtained from the Editor.

server in space, exhibits a different contrast, which is referred to as the apparent contrast. This change in contrast, due to a change in the relative position of the observer, is due to the differences in the manner in which the atmospheric screen affects these two signals.

The ratio of the apparent to the intrinsic contrast of an object, as seen from a satellite through an atmospheric screen and as seen at the ground level, respectively, is a quantity independent of the reflection characteristics of the object and of the directional characteristics of the field of illumination. (For the mathematical definitions, see the next section.) This quantity, referred to in this paper as the contrast attenuation factor, seems to have been introduced by Duntley et al. [8], who called it a contrast transmission factor. A mathematical definition of this quantity is given by these authors; however, no theoretical values are provided for any atmospheric conditions.

Fraser [9] referred to the aforementioned quantity as the contrast attenuation coefficient and computed its values for several selected wavelengths and solar zenith angles. Because of the unavailability both of current methods that could solve the radiative transfer equation for nonhomogeneous atmospheric models, and of adequate computing resources, Fraser's study was primarily restricted to a nonabsorbing Rayleigh atmosphere. His turbid atmospheric models contained an exponential decrease with height of nonabsorbing aerosol particles. Only primary scattering of direct solar radiation by aerosols was taken into account and this in an approximate manner. However, Fraser seems to be the first investigator to point out that the apparent contrast of an object can be significantly enhanced by rotating an analyzer in front of a satellite optical system. This study by Fraser was restricted to atmospheric models resting on a ground obeying Lambert's law of reflection. Coulson's [10] measurements showed that radiation reflected by many natural surfaces exhibits partial polarization. He then used his reflection measurements to compute contrast attenuation factors for several natural surfaces viewed through nonabsorbing Rayleigh atmospheres.

In this paper, results of a theoretical study are presented that show the dependence of the contrast attenuation factor on atmospheric composition, wavelength, sun angle, ground reflectivity, and on the nadir as well as azimuth angles of view. The atmospheric models used vary from an aerosol-free model without any gaseous absorption to several models with absorption by common absorbing gases and moderate to high concentrations of spherical dust particles. These models, representing the average, midlatitude summer conditions, are assumed to

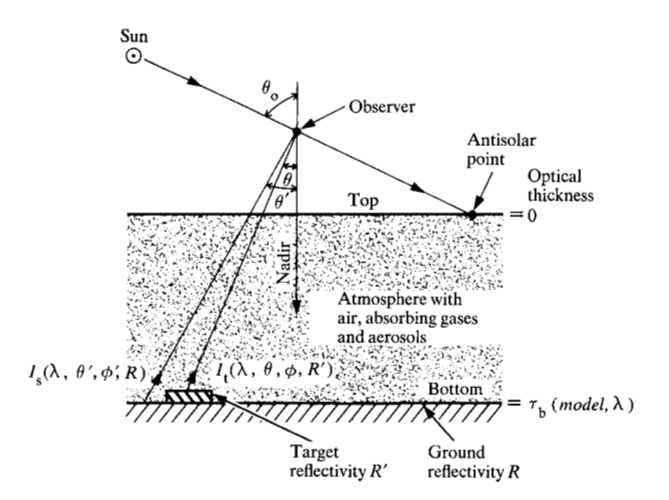


Figure 1 Schematic of the observation geometry.

rest on a ground obeying Lambert's law of reflection. A scalar form (i.e., neglecting the polarization characteristics of scattered radiation) of the radiative transfer equation for a plane-parallel, nonhomogeneous atmosphere with scattering and absorption is used for this purpose. Some thoughts about future work aimed at correcting actual satellite data are expressed in the last section.

Necessary expressions

Let us consider a plane-parallel model of the terrestrial atmosphere illuminated by a plane-parallel beam of the monochromatic solar radiation of wavelength λ micrometers, at an angle of θ_0 degrees with respect to the local zenith (Fig. 1). The amount of energy in a one-micrometer wavelength interval, passing per second through a onesquare-meter area normal to the direction of incidence at the top, is taken to be $I_{o\lambda}$ (W/m²- μ m). The plane-parallel model means that the model is of homogeneous character and of infinite extent along the horizontal directions. Any nonhomogeneity due to scattering and/or absorption by molecules as well as aerosols (e.g., dust particles assumed to exist in the form of a spherical polydispersion of a material with known refractive index) is confined to the vertical direction only. We further assume that this atmospheric model rests on a ground obeying Lambert's law of reflection. Accordingly, a fraction R (Lambert reflectivity) of the total radiation incident upon the ground is isotropically reflected by it, independent of the distribution and polarization characteristics of the radiation incident upon it. This model is characterized by two parameters, namely, the atmospheric composition including the surface pressure (represented by a unique model number), and the wavelength \(\lambda \). These two parameters can be combined in a single parameter $\tau_{b}(model, \lambda)$ which is the

Table 1 Normal optical thickness due to molecular scattering for models 1 through 5 and due to aerosol scattering and absorption for models 3 and 5 for selected wavelengths.

Wavelength (µm)	Models I to 5 molecular scattering	Model 3 aerosol scattering	Model 3 aerosol absorption	Model 5 aerosol scattering	Model 5 aerosol absorption
0.3100	1.0610	0.08159	0.01344	0.03662	0.00997
0.3950	0.3825	0.08696	0.01139	0.03928	0.00880
0.4950	0.1508	0.09039	0.00959	0.04179	0.00774
0.5950	0.07119	0.09107	0.00821	0.04371	0.00690
0.7400	0.02941	0.08836	0.00671	0.04555	0.00595

total, normal optical thickness of the model. See Table 1 for normal optical thicknesses due to molecular and aerosol scattering and aerosol absorption for the different models at selected wavelengths. A ray passing completely through the model along the vertical direction suffers an attenuation of $\exp \left[-\tau_h(model, \lambda)\right]$.

Let $I_s(model, \lambda, \theta_o, \theta', \phi', R)$ be the specific intensity (or radiance) of the radiation reflected by the ground in the direction θ' , ϕ' , where θ' is the angle referred to the local zenith, and ϕ' is the azimuth angle with respect to the sun's meridian plane, i.e., the vertical plane passing through the sun and the observer. This specific intensity resulting from reflection of the direct solar and diffuse atmospheric radiation at the ground level is measured in W/m^2 - μ m-sterad. For the case of the Lambertian reflection, this radiation can be represented by $I_g(model, \lambda, \theta_o, R)$. The radiation received by the observer in the direction θ' , ϕ' is then given by

$$I'_{s}(model, \lambda, \theta_{o}, \theta', \phi', R)$$

$$= I_{g}(model, \lambda, \theta_{o}, R) \exp(-\tau_{b} \sec \theta')$$

$$+ AR(\theta', \phi'), \qquad (1)$$

where AR stands for the atmospheric radiation resulting from the scattering of the unidirectional solar radiation and the diffuse ground-reflected radiation illuminating the atmosphere from above and below. It also depends upon the remaining four parameters, namely, the model, λ , $\theta_{\rm o}$, and R.

We next consider a small target reflecting the direct as well as the diffuse radiation incident upon it according to some arbitrary law of reflection such that its reflectivity R' is a function of several directional parameters. The smallness of the target implies that it does not modify any features of the atmospheric radiation field in any significant manner, except for the view direction represented by θ , ϕ . Let $I_{\rm t}$ (model, λ , $\theta_{\rm o}$, θ , ϕ , R') represent the specific intensity of the radiation reflected by the target in the di-

rection θ , ϕ . The radiation received by the observer in the direction θ , ϕ is then given by

$$I'_{t}(model, \lambda, \theta_{o}, \theta, \phi, R')$$

$$= I_{t}(model, \lambda, \theta_{o}, \theta, \phi, R') \exp(-\tau_{b} \sec \theta)$$

$$+ AR(\theta, \phi). \tag{2}$$

Intrinsic and apparent contrasts of the object are then given respectively by

$$\begin{split} &C_{\mathrm{i}}(model,\,\lambda,\,\theta_{\mathrm{o}},\,\theta,\,\phi,\,R,\,R')\\ &=\frac{I_{\mathrm{t}}(model,\,\lambda,\,\theta_{\mathrm{o}},\,\theta,\,\phi,\,R')\,-\,I_{\mathrm{g}}(model,\,\lambda,\,\theta_{\mathrm{o}},\,R)}{I_{\mathrm{g}}(model,\,\lambda,\,\theta_{\mathrm{o}},\,R)}, \quad (3) \end{split}$$

and

$$\begin{split} &C_{\mathrm{a}}(model,\,\lambda,\,\theta_{\mathrm{o}},\,\theta,\,\phi,\,R,\,\theta',\,\phi',\,R')\\ &=\frac{I'_{\mathrm{t}}(model,\,\lambda,\,\theta_{\mathrm{o}},\,\theta,\,\phi,\,R')}{I'_{\mathrm{s}}(model,\,\lambda,\,\theta_{\mathrm{o}},\,\theta',\,\phi',\,R)}\\ &-\frac{I'_{\mathrm{s}}(model,\,\lambda,\,\theta_{\mathrm{o}},\,\theta',\,\phi',\,R)}{I'_{\mathrm{s}}(model,\,\lambda,\,\theta_{\mathrm{o}},\,\theta',\,\phi',\,R)} \;. \end{split} \tag{4}$$

Since the target is assumed to be small, $AR(\theta, \phi)$ is practically equal to $AR(\theta', \phi')$. Hence, θ', ϕ' symbols in the representation of C_a can be omitted. After making use of Eqs. (1)-(3) and taking $\theta = \theta'$ and $\phi = \phi'$, we can rewrite Eq. (4) as

$$C_{a}(model, \lambda, \theta_{o}, \theta, \phi, R, R')$$

$$= A(model, \lambda, \theta_{o}, \theta, \phi, R)$$

$$\times C_{i}(model, \lambda, \theta_{o}, \theta, \phi, R, R'), \tag{5}$$

where the contrast attenuation factor $A(model, \lambda, \theta_0, \theta, \phi, R)$ is given by

$$A(model, \lambda, \theta_{o}, \theta, \phi, R) = \frac{I_{g}(model, \lambda, \theta_{o}, R) \exp(-\tau_{b} \sec \theta)}{I'_{s}(model, \lambda, \theta_{o}, \theta, \phi, R)}.$$
(6)

216

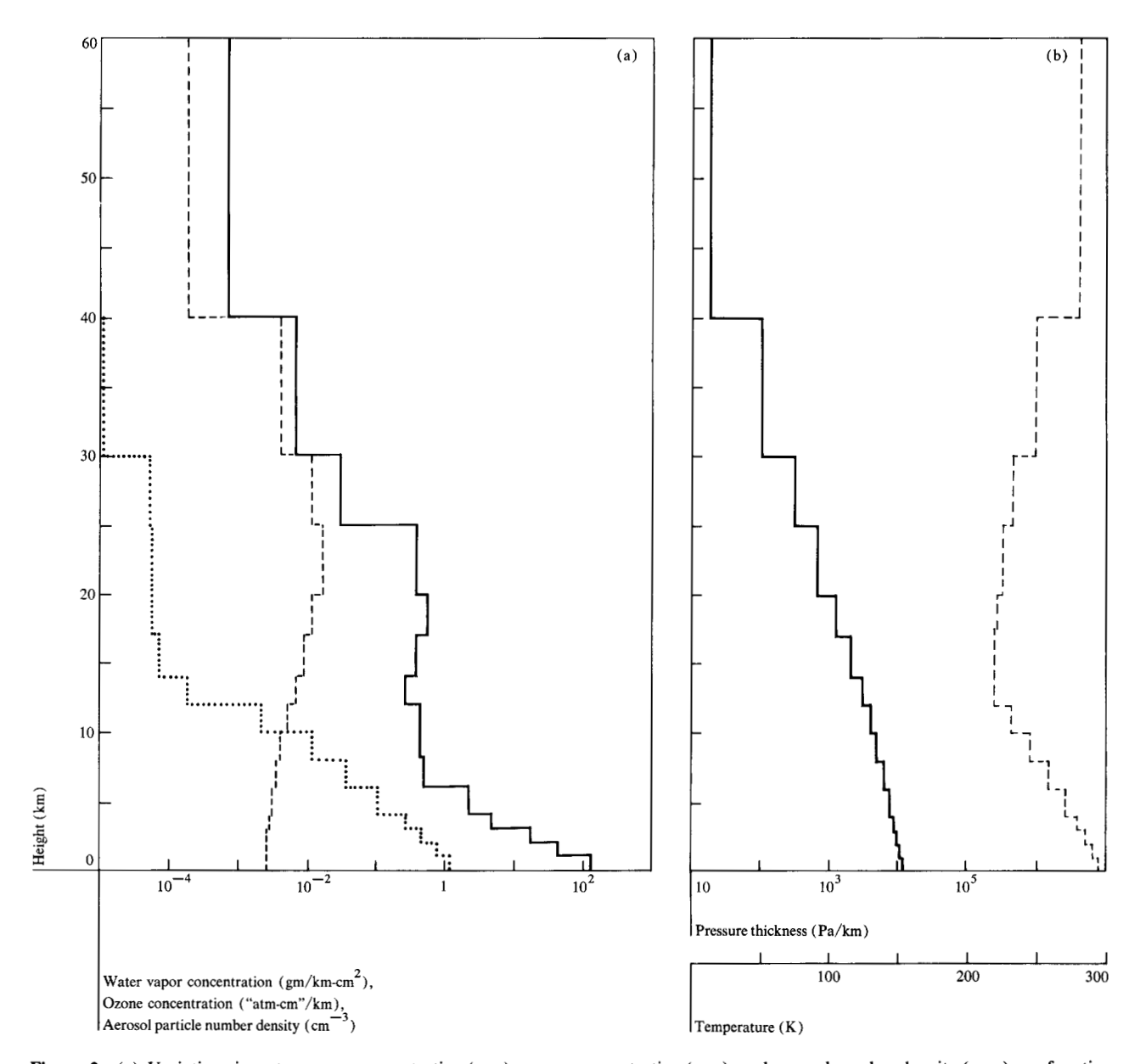


Figure 2 (a) Variations in water vapor concentration $(\cdot \cdot \cdot)$, ozone concentration $(\cdot \cdot \cdot)$, and aerosol number density (---) as a function of height. (b) Variations of pressure thickness (---) and temperature (---) with height. The aerosol-height distribution shown is for a total of 19.815×10^6 particles in a vertical column of 1-cm^2 cross section, i.e., the distribution for model number 3. Distributions for models 4 and 5 are obtained after multiplying the aerosol number density of all layers by an appropriate constant. The data are for the midlatitude summer model.

It may be noted that the intrinsic contrast as defined by Eq. (3) goes to infinity as R approaches zero. Under such circumstances, the contrast attenuation factor defined by Eq. (6) goes to zero, and the apparent contrast as defined by Eq. (5) becomes indeterminate. One is then required to use Eq. (4); see Ref. [9].

Computations

Values of $I_{\rm g}(model,\lambda,\theta_{\rm o},R),\tau_{\rm b}$, and $I_{\rm s}'(model,\lambda,\theta_{\rm o},\theta,\phi,R)$ are easily obtainable for a number of combinations of

the aforementioned parameters from radiation datasets we have generated [11]. (These computations were performed by taking into account all orders of scattering.) By using these radiation datasets, values of the contrast attenuation factor defined by Eq. (6) were calculated for the five different atmospheric models described in the next section, and for the following values of the remaining five parameters.

 λ : 38 unequally spaced wavelengths in the spectral range 0.31-0.9935 μ m; see Ref. [11] for the exact val-

217

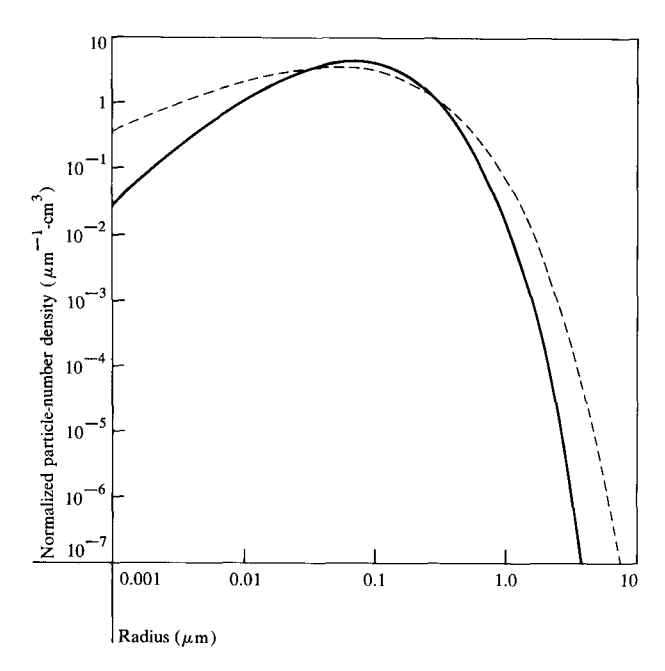


Figure 3 Variations in the normalized aerosol number density as a function of the particle radius for two size distribution functions, Haze L (——) and Haze M (- - -). The area under a given curve is equal to 1 particle/cm³.

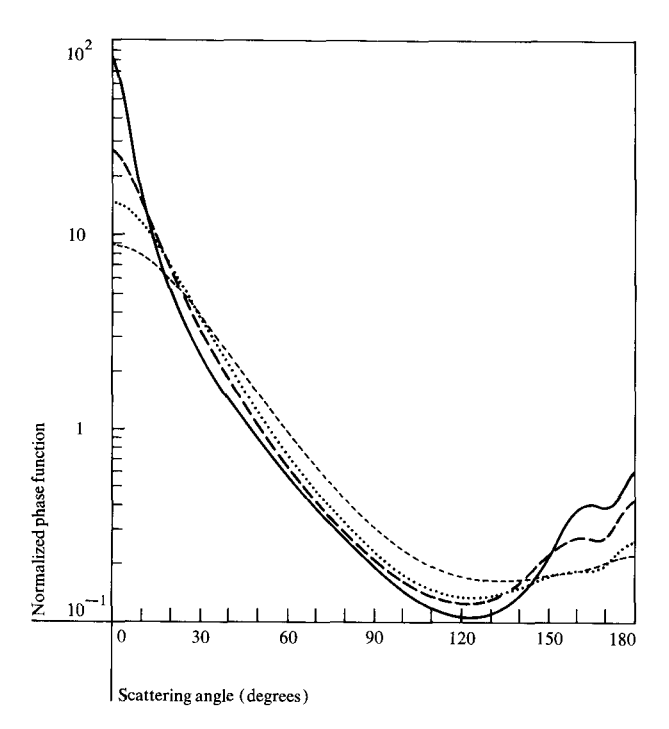


Figure 4 Variations in the normalized phase function of a unit volume of the spherical polydispersion Haze L as a function of the scattering angle. Different curves are for wavelengths of 0.3100 (——), 0.6150 (———), 1.1085 (···), and 2.0050 μ m (---). The refractive index is taken as 1.5-0.01 *i*. An integration of the scattering phase function over a solid angle of 4π yields a value of 4π .

ues. Wavelengths are unequally spaced in order to simulate the absorption bands of oxygen, ozone, and water vapor.

 θ_{\circ} : 0°, 30°, 45°, 60°, 70°, 75°, and 80°.

 θ : 0°, 30°, and 60°.

 ϕ : 0°, 10°, · · · , 180°.

 $R: 0.1, 0.2, \cdots, 0.8.$

Atmospheric models

As mentioned earlier, the atmospheric models selected for our investigations are plane-parallel in nature. All five models are cloudfree and have a surface measure of 101.3 kPa (1013 mb). The first model is free of aerosols and absorbing gases, but the remaining four models contain 0.308 atm-cm of ozone, 2.96 gm-cm⁻² of water vapor, and absorption due to oxygen in the appropriate spectral intervals. These models, based on actual data from Ref. [12], are for average cloudfree conditions encountered during summer months over midlatitude regions. Further information about the vertical profile of aerosols, ozone [13], water vapor, and temperature as used in our investigations can be found in Figs. 2(a) and (b). (Figs. 2-6 are taken from Ref. [11].)

Information about the aerosol content and size distribution characteristics of aerosols in various models is provided in Table 2. These aerosol particles are assumed to exist, in the model, in the form of a spherical polydispersion of material with a spectrally independent refractive index of 1.5-0.01 i. Size distribution characteristics of the spherical polydispersions Haze L and Haze M, specified in column 4 of Table 2, can be found in Fig. 3. It is sufficient to state here that the Haze L distribution is representative of the conditions encountered in the lower atmosphere over large continental areas, while the Haze M distribution is for those encountered near coastal regions [14]. The total aerosol contents of 1-cm² cross sections (see Table 2) for models 3 and 4 simulate conditions of average and strong turbidity, respectively. Models 3 and 5 contain aerosols with different size distribution characteristics, but have the same amount of aerosol mass loading per unit horizontal area. However, since the Haze M distribution contains a greater number of large particles than the Haze L distribution, model 5 is less turbid than model 3. Further information about the optical properties of various models can be found in Figs. 4-6.

Discussion of results

Wavelength dependence

Values of the contrast attenuation factor $A(model, \lambda, \theta_o, \theta, \phi, R)$ defined by Eq. (6) are plotted as a function of

Table 2 Basic information about various atmospheric models; refractive index of the aerosol material = 1.5-0.01 i.

	Gaseous absorption	Total number of aerosol particles in a column of 1-cm² cross section	function of
1	No	-	_
2	Yes	_	_
3	Yes	19.815×10^{6}	Haze L
4	Yes	99.075×10^6	Haze L
5	Yes	4.673×10^{6}	Haze M

wavelength (λ in μ m) in Figs. 7(a)-(c) for the solar zenith angle $\theta_o = 0^\circ$, 45°, and 80°, respectively. These contrast attenuation factors are for the nadir viewing direction, i.e., $\theta = \phi = 0^\circ$. Solid curves represent results for the atmospheric models resting on a Lambertian ground with R = 0.1, while the results for model 2 appear as a dotted curve. Results for models 1 and 4 with an underlying Lambertian ground reflectivity of 0.8 are given by the dashed curves. In some cases, parts of the curves are omitted for clarity.

For the atmospheric model free of any gaseous absorption and aerosols (model 1), $A(1, \lambda, \theta_0, 0, 0, 0.1)$ increases rapidly with an increase of λ for all three values of θ_0 . There is also some θ_0 dependence; for example, the contrast attenuation factor is equal to 0.064, 0.053, and 0.027 at $\lambda = 0.31$; it is equal to 0.963, 0.961, and 0.903 at $\lambda =$ $0.9935 \ \mu m$ for $\theta_0 = 0^{\circ}$, 45°, and 80°, respectively. These very strong decreases in the contrast attenuation factor with a decrease in wavelength are due to the fact that the scattering cross section of a molecule increases inversely as the fourth power of the wavelength (Rayleigh law of scattering). Results for model 2 (dotted curve) show several significant deviations from those for model 1. The depressions in the $A(2, \lambda, 0, 0, 0, 0.1)$ vs λ curve [Fig. 7(a)] at $\lambda = 0.725$, 0.825, and 0.947 μ m are due to absorption by atmospheric water vapor, while that at $\lambda = 0.7625 \,\mu\text{m}$ is due to absorption by oxygen. Effects due to absorption by ozone are visible in the spectral range 0.31-0.33 μ m. An increase in θ_0 from 0° to 80° [Figs. 7(a)-(c)] results in strong accentuation of the absorption features. In addition, the effect of absorption by ozone in the visible region (Chappuis band, 0.53-0.66 µm) is clearly evident in the results presented in Fig. 7(c) for $\theta_0 = 80^{\circ}$. (It should be pointed out that the radiation computations in the spectral bands of absorption by oxygen and water vapor involve several assumptions. For further information on this subject, the reader is referred to Ref. [11]).

An increase in the atmospheric aerosol content results in a sharp decrease in the contrast attenuation factor. For average nonsummer observation geometry for Landsat

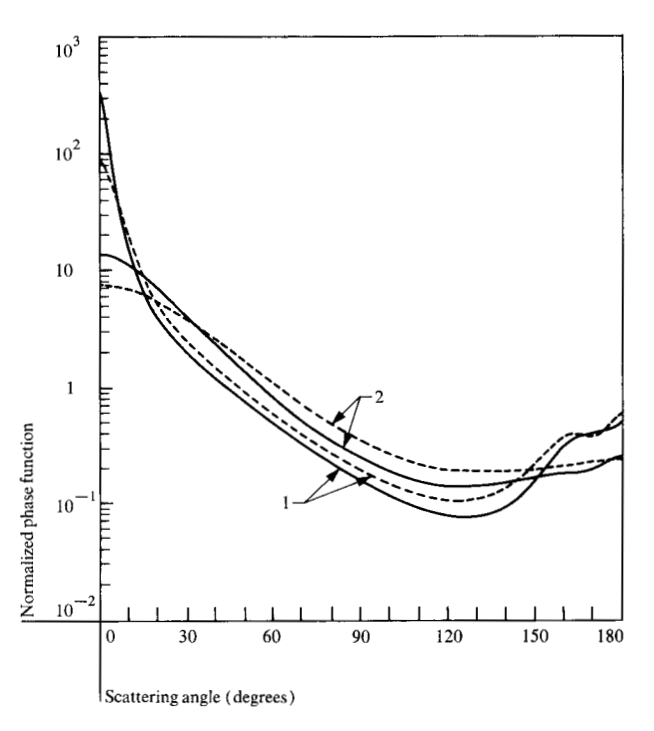


Figure 5 Variations in the normalized phase function of a unit volume of the spherical polydispersions Haze L (- - -) and Haze M (——) as a function of scattering angle for incident radiation wavelengths of (1) 0.3100 and (2) 2.4500 μ m; refractive index equals 1.5-0.01 *i*. An integration of the scattering phase function over a solid angle of 4π yields a value of 4π .

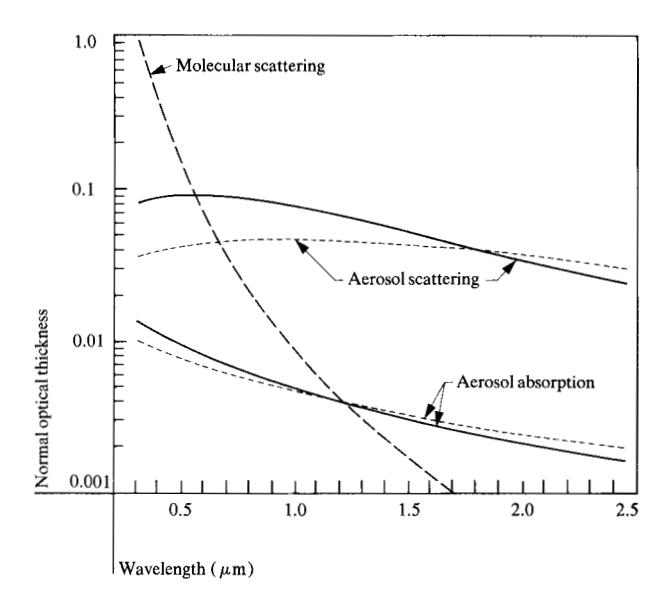


Figure 6 Variations in the normal optical thickness for molecular scattering, aerosol scattering, and aerosol absorption as functions of the wavelength of incident radiation for models 1 to 5 (— —); model 3 (——); model 5 (- - -). Aerosol normal optical thicknesses for model 4 are obtained after multiplying the corresponding values for model 3 by five.

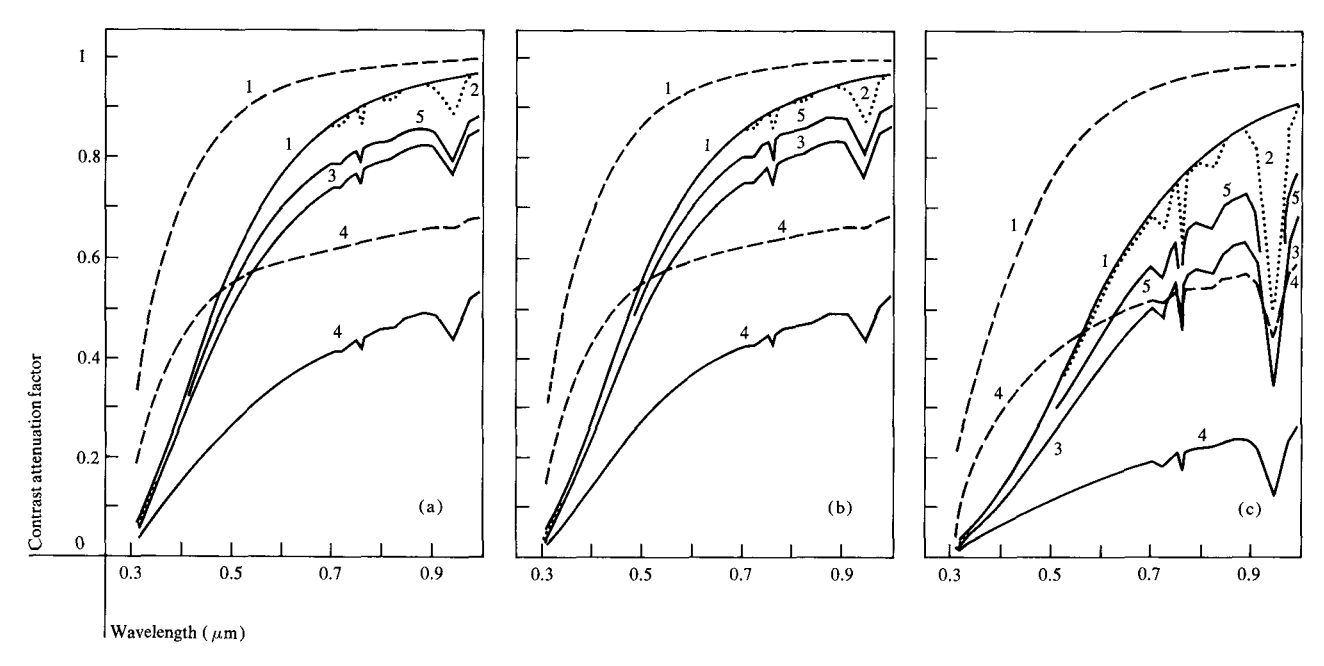


Figure 7 Variations in the contrast attenuation factor as a function of wavelength for different atmospheric models resting on a Lambertian ground with reflectivity R=0.1 (—— and · · · ·) and 0.8 (- · -); (a) $\theta_0=\theta=\phi=0^\circ$, (b) $\theta_0=45^\circ$, and $\theta=\phi=0^\circ$, and (c) $\theta_0=80^\circ$, and $\theta=\phi=0^\circ$.

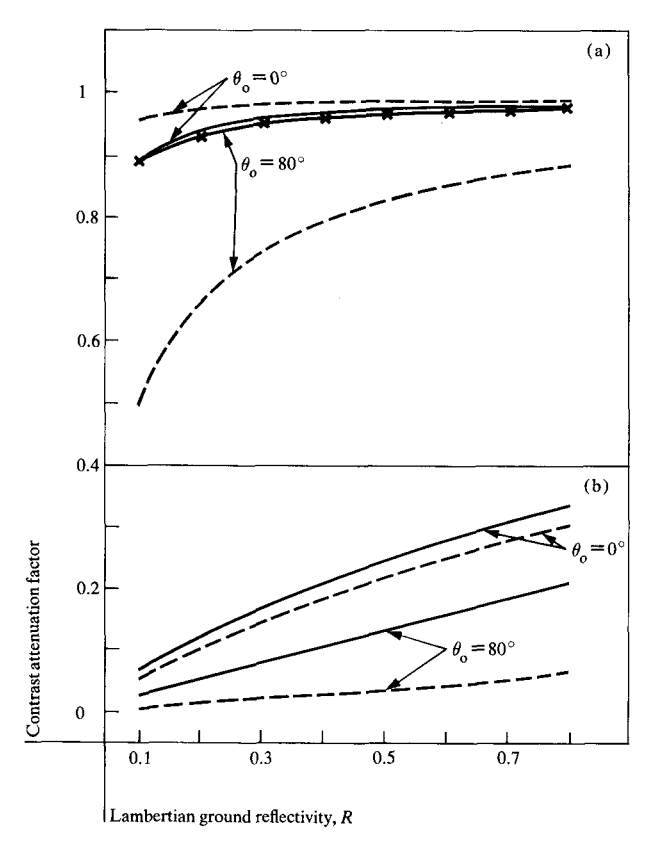


Figure 8 Variations in the contrast attenuation factor as a function of the Lambertian reflectivity R of the ground underlying the atmospheric model; $\theta_0 = 0^\circ$ and 80° ; $\theta = \phi = 0^\circ$. Models 1 (—— and xxx) and 2 (- - -); (a) 0.947 μ m and (b) 0.31 μ m.

satellites over a midlatitude region [Fig. 7(b)], an increase in the atmospheric turbidity from zero to average to strong (models 2 through 4) results in a decrease in the contrast attenuation factor from 0.939 to 0.830 to 0.488, respectively, at $\lambda = 0.889 \, \mu \text{m}$. Absorption features due to atmospheric gases become less prominent with increases in atmospheric turbidity. A change in the size distribution function from Haze L to Haze M without any change in aerosol mass loading (coagulation among aerosol particles, models 3 to 5), results in an increase in the contrast attenuation factor.

An increase in ground reflectivity from 0.1 to 0.8 (solid and dashed curves for models 1 and 4) results in an increase in the contrast attenuation factors, and associated strong dampening of the gaseous absorption features at high sun angles [Figs. 7(a) and (b)]. This R dependence of $A(model, \lambda, \theta_0, 0, 0, R)$ in two spectral regions of gaseous absorption is compared in Fig. 8 for $\lambda = 0.31$ and 0.947 μ m, for $\theta_0 = 0^{\circ}$ and 80°, and for models 1 (solid curves) and 2 (dotted curves). Curves for both wavelengths exhibit somewhat similar trends for $\theta_0 = 0^\circ$. On the other hand, differences between the contrast attenuation factors at $\theta_0 = 80^{\circ}$ for models 1 and 2 increase from 0.020 to 0.146 at $\lambda = 0.31 \,\mu\text{m}$, but decrease from 0.390 to 0.095 at $\lambda = 0.947 \ \mu \text{m}$ as R is increased from 0.1 to 0.8. These differences are due to changes in the relative importance of directly transmitted and diffuse atmospheric radiations [see Eq. (1)].

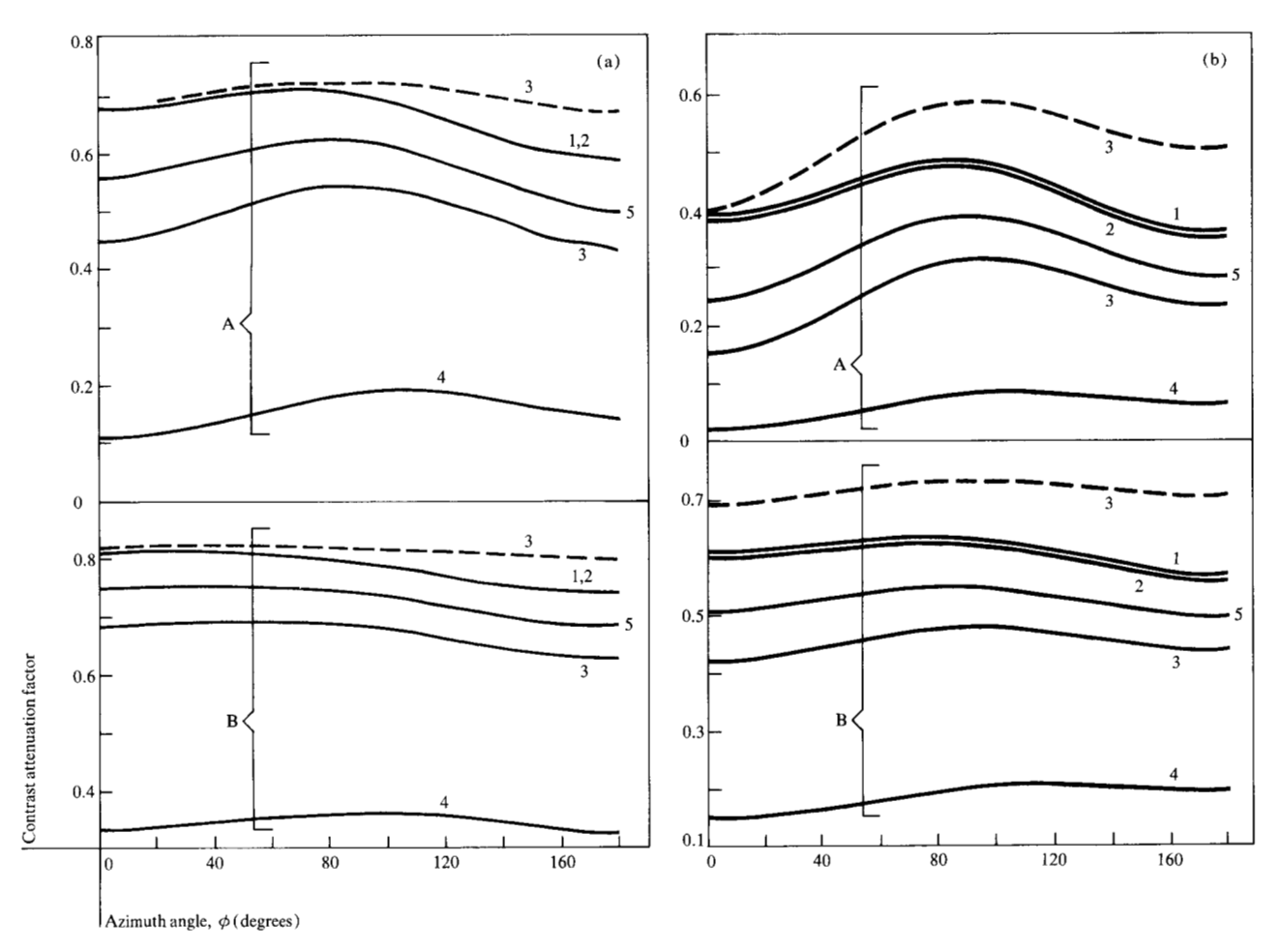


Figure 9 Variations in the contrast attenuation factor as a function of ϕ (with reference to the sun's meridian plane) and θ_0 ; nadir angles of view, θ , equal to (curves A) 60° , and (curves B) 30° . Different curves are for different atmospheric models resting on a Lambertian ground with reflectivity R=0.2 (——) and 0.8 (- - -) at $\lambda=0.595$ μm ; (a) $\theta_0=60^\circ$ and (b) $\theta_0=80^\circ$.

Table 3 Contrast attenuation factors for the five atmospheric models for $\theta_0 = 30^\circ$, 60° , and 80° ; $\lambda = 0.595 \,\mu\text{m}$, R = 0.2, and $\phi = 0^\circ$.

Model number	$\theta_{\rm o} = 30^{\rm o}$			$\theta_{\rm o} = 60^{\rm o}$		$\theta_{\rm o} = 80^{\rm o}$			
	$\theta = 0^{\circ}$	$\theta = 30^{\circ}$	$\theta = 60^{\circ}$	$\theta = 0^{\circ}$	$\theta = 30^{\circ}$	$\theta = 60^{\circ}$	$\theta = 0^{\circ}$	$\theta = 30^{\circ}$	$\theta = 60^{\circ}$
1	0.843	0.853	0.788	0.813	0.813	0.672	0.664	0.613	0.394
2	0.842	0.853	0.788	0.812	0.813	0.671	0.660	0.608	0.388
3	0.751	0.756	0.628	0.715	0.687	0.446	0.524	0.424	0.159
4	0.471	0.451	0.242	0.414	0.335	0.108	0.244	0.151	0.028
5	0.797	0.806	0.708	0.765	0.752	0.555	0.590	0.510	0.249

Directional dependence

We now discuss the θ and ϕ dependences of the contrast attenuation factor for selected values of θ_0 and λ . Values of $A(model, 0.595, \theta_0, \theta, 0.2)$ for $\theta = 0^{\circ}, 30^{\circ}$, and 60° , and for $\theta_0 = 30^{\circ}, 60^{\circ}$, and 80° are given in Table 3 for all five atmospheric models listed in Table 2. It can be

seen that the contrast attenuation factor decreases with an increase in θ , θ_o , and the atmospheric turbidity.

Values of $A(model, 0.595, \theta_0, \theta, \phi, R)$ for $\theta = 30^{\circ}$ and 60° are plotted as a function of the azimuth angle ϕ in Figs. 9(a) and (b) for $\theta_0 = 60^{\circ}$ and 80°, respectively. Re-

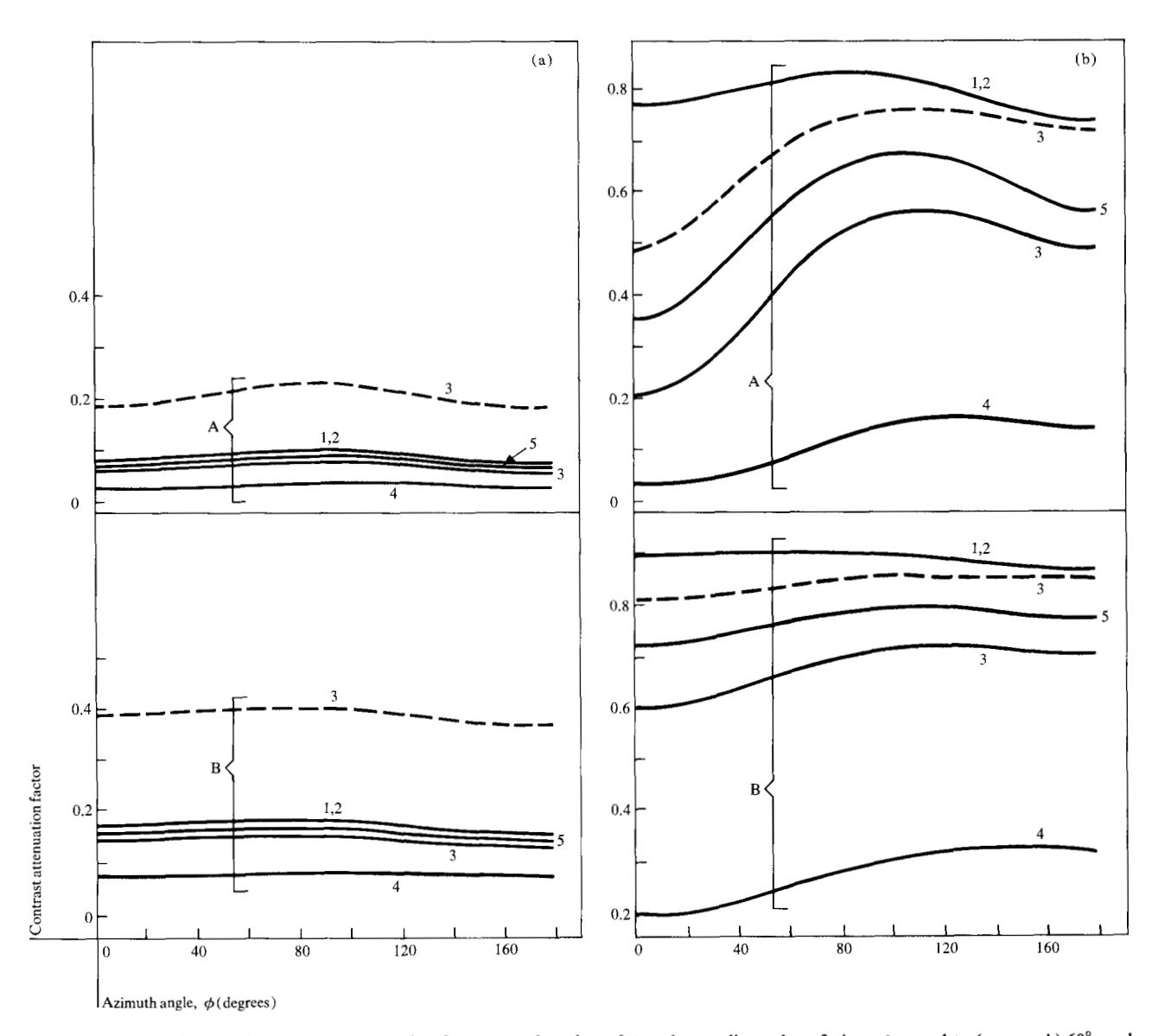


Figure 10 Variations in the contrast attenuation factor as a function of ϕ and λ ; nadir angles of view, θ , equal to (curves A) 60° , and (curves B) 30° . Different curves are for models and R values as in Fig. 9; (a) $\lambda = 0.395 \ \mu m$ and (b) $\lambda = 0.8675 \ \mu m$.

sults for R=0.2 (R=0.8) are shown by the solid (dashed) lines. For R=0.8, only the results for model 3 are presented. Almost all curves exhibit a maximum in the range of 70° to 110°. Furthermore, this maximum achieves the greatest sharpness at large θ and θ_0 . For example, for $\theta_0=80^\circ$, $\theta=60^\circ$, R=0.2, and model 3, A decreases by a factor of 2 as the azimuth angle of view is changed from 90° to 0°. Results similar to those presented in Fig. 9(b) but for $\lambda=0.395$ and 0.8675 μ m are shown in Figs. 10(a) and (b), respectively. Both of these wavelengths are in the spectral regions located outside the absorption bands

of common atmospheric gases. A decrease in the wavelength from 0.595 to 0.395 μ m results in a substantial flattening of the A vs ϕ curves. On the other hand, an increase in wavelength from 0.595 to 0.8675 μ m results in a strong increase in the azimuthal dependence of the contrast attenuation factor.

Concluding remarks

In the preceding sections, the contrast attenuation factor was defined as the ratio of the apparent contrast of an object as seen through the atmospheric screen from a satellite, to its intrinsic contrast when viewed at the surface of the earth. Dependence of this factor was then theoretically examined for six different parameters. For this purpose, computed values of the radiation scattered by plane-parallel but nonhomogeneous, realistic models of the cloudfree, midlatitude summer atmosphere were used [11]. These radiation calculations were performed after consideration of all orders of scattering in the models. Selected results were presented to show the strong dependence of the contrast attenuation factor on wavelength, atmospheric aerosol content or turbidity, size distribution characteristics of aerosols, gaseous absorption, Lambertian reflectivity of the ground, the sun's position, and the nadir as well as the azimuth angles of observation.

For ideal conditions (no aerosols in the atmosphere) the contrast attenuation factor near the 1.0-µm wavelength region lies between 0.9 and 1.0, depending upon the exact value of the wavelength, the ground reflectivity, and the sun's position, provided the directions of observation are confined fairly close to the local nadir. Thus, Landsat observations in the $0.8-1.1-\mu m$ spectral band are frequently used in many applications. However, our results show that a moderate-absorption band of water vapor is located in the middle of this Landsat spectral band. Water vapor content of an atmospheric column is highly variable, and furthermore, its effect on the contrast attenuation factor is modulated by ground reflectivity and by aerosols. Hence, corrections of the 0.8-1.1-µm band Landsat data are often made by users. Such corrections are probably based on the ground-truth and other related information, and can also be based on the experience of the user and his familiarity with the scene. This aspect of data analysis is rarely discussed in the open literature. Results of our investigation can assist in our understanding of this problem in a more quantitative manner.

A meaningful correction of Landsat data in the other three spectral bands is a very complex, multi-parameter problem. Some of these parameters are strongly dependent on space and time, with very little information available at the point and time of the observations of interest. Hence, several valid questions are raised concerning the practical usefulness of such theoretical investigations in real-life situations. Our present investigation is not complete in the sense that it does not encompass ranges of various parameters such as ozone amount, water vapor amount, possible refractive indices of the aerosol material, and size distribution characteristics of aerosols. Furthermore, as pointed out during the discussion of results, the spectral regions of absorption by water vapor and other gases require a much more detailed examination than the one performed for the present study. The work reported by the author in Ref. [11] was carried out with a

very reasonable amount of computing resources. Hence, no difficulties can be foreseen in generating similar but more sophisticated and extensive datasets which can be used for understanding the problem in a very comprehensive manner. They can also be used, in the first approximation, for providing contrast attenuation information for the models resting on a surface with variable albedo, e.g., a large plantation or farm surrounded by bare land, or an island.

As for correcting the real-life data, two approaches come to our mind at this time. Santisteban and Muñoz [15] point out the possibility of a great degree of redundancy in the Landsat data under several circumstances. If so, some of these redundant observations can be used to provide information about the contrast attenuation factor at the scene. Several investigators [16, 17] have suggested correction of satellite data by means of ground-based radiation observations at strategic points and times. Our radiation datasets [11] provide an excellent opportunity for detailed examination of such a complementary technique for various atmospheric conditions and observational geometries.

Finally, such theoretical investigations involving other computational procedures [18] can be extended to study the feasibility of using polarization measurements for remote sensing of terrestrial features [9]. Radiation reflected by many surfaces is polarized [10], and the atmospheric screen would affect the parallel and perpendicular components of the signal differently. In some cases, elliptical polarization may be detected which can be used with advantage in the analysis of data.

References and note

- ERTS Data Users Handbook, NASA 715D4249, NASA Goddard Space Flight Center, Greenbelt, MD.
- Proceedings of the Third Earth Resources Technology Satellite-1 Symposium, December 1973, NASA SP-351, compiled and edited by S. C. Freden, E. P. Mercanti, and M. A. Becker, NASA Goddard Space Flight Center, Greenbelt, MD.
- 3. Abstracts of the NASA Earth Resources Survey Symposium, June 1975, NASA Johnson Space Center, Houston, TX.
- 4. R. Bernstein, "Digital Image Processing of Earth Observation Sensor Data," *IBM J. Res. Develop.* 20, 40 (1976).
- R. H. Kidd and R. H. Wolfe, "Performance Modeling of Earth Resources Remote Sensors," *IBM J. Res. Develop.* 20, 29 (1976).
- W. A. Malila, R. B. Crane, C. A. Omarzu, and R. E. Turner, "Studies of the Spectral Discrimination," NASA Contract No. NAS9-9784, May 1971, Willow Run Laboratories, University of Michigan, Ann Arbor, MI.
- J. V. Dave, P. A. Sheppard, and C. D. Walshaw, "Ozone Distribution and the Continuum from Observations in the Region of the 1043 cm⁻¹ Band," *Quart. J. Roy. Meteorol. Soc.* 89, 307 (1963).
- S. Q. Duntley, A. R. Boileau, and R. W. Preisendorfer, "Image Transmission by the Troposphere, I," J. Opt. Soc. Amer. 47, 499 (1957).

- R. S. Fraser, "Apparent Contrast of Objects on the Earth's Surface as Seen from Above the Earth's Atmosphere," J. Opt. Soc. Amer. 54, 289 (1964).
 K. L. Coulson, "Effects of Reflection Properties of Natural
- K. L. Coulson, "Effects of Reflection Properties of Natural Surfaces in Aerial Reconnaissance," Appl. Opt. 5, 905 (1966).
- 11. J. V. Dave, "Extensive Datasets of the Diffuse Radiation in Realistic Atmospheric Models with Aerosols and Common Absorbing Gases," Solar Energy 21, 361 (1978).
- R. A. McClatchey, R. W. Fenn, J. E. A. Selby, J. S. Garing, and F. E. Volz, "Optical Properties of the Atmosphere," *Technical Report No. AFCRL-70-0527*, Air Force Cambridge Research Laboratories, Bedford, MA, 1970.
- The units of "atm-cm"/km for the ozone concentrations are defined in W. L. Godson, "Representation and Analysis of Vertical Distributions of Ozone," Quart. J. Roy. Meteorol. Soc. 88, 220 (1962).
- 14. D. Deirmendjian, Electromagnetic Scattering on Spherical Polydispersions, American-Elsevier, New York, 1969.
- A. Santisteban and L. Muñoz, "Principal Components of a Multispectral Image: Application to a Geological Problem," IBM J. Res. Develop. 22, 444 (1978).

- J. I. Gordon, J. L. Harris, Sr., and S. Q. Duntley, "Measuring Earth-to-Space Contrast Transmittance from Ground Stations," Appl. Opt. 12, 1317 (1973).
- K. Peacock, "Ground-Based Determination of Atmospheric Radiance for Correction of ERTS-1 Data," Appl. Opt. 13, 2741 (1974).
- J. V. Dave, "Development of Programs for Computing Characteristics of Ultraviolet Radiation, Technical Report— Vector Case," Programs 1-4, NASA Contract No. NASS-21680, 1972, IBM Federal Systems Division, Gaithersburg, MD.

Received October 11, 1978; revised October 20, 1978

The author is located at the IBM Data Processing Scientific Center, 1501 California Avenue, Palo Alto, California 94304.